

Spectroscopy of a Cooper-Pair box in the Autler-Townes configuration

E. J. Griffith* and J. F. Ralph

*Department of Electrical Engineering and Electronics,
The University of Liverpool, Brownlow Hill, Liverpool, L69 3GJ, United Kingdom.*

Andrew D. Greentree

*The Centre for Quantum Computer Technology, School of Physics,
The University of Melbourne, Victoria 3010, Australia.*

T. D. Clark

*Centre for Physical Electronics and Quantum Technology,
The University of Sussex, Falmer, Brighton, BN1 9QT, United Kingdom.*

(Dated: December 2, 2024)

Abstract: A spectroscopic analysis of a microwave driven superconducting charge qubit (Cooper pair box) coupled to an LC oscillator is performed. By treating the oscillator as a probe through the backreaction effect of the qubit on the oscillator circuit, we extract frequency splitting features analogous to the Autler-Townes effect from quantum optics, thereby extending the analogies between superconducting and quantum optical phenomenology. These features are found in a frequency band that avoids the need for complicated high frequency measurement systems and therefore may be of use in qubit characterisation and novel coupling schemes. In addition we find this frequency band can be adjusted to suit an experimental frequency regime by changing the oscillator frequency.

PACS numbers: 03.65.-w, 74.50.+r, 85.25.Dq

Keywords: Autler Townes effect, charge qubit, characterisation, frequency spectrum

I. INTRODUCTION

Superconducting charge qubits (Cooper pair boxes) are promising candidates for use in quantum information processing and quantum computing systems. Many of the necessary results for quantum computing have already been demonstrated in these systems including single qubit rotations [1, 2], single-shot readout [3] and two-qubit entanglement [4].

In common with other solid-state technologies (e.g. Si:P [5]), superconducting devices are expected to be highly scalable due to the ability to construct large numbers of qubits using existing lithographic manufacturing [6]. However, any lithographic procedure has intrinsic manufacturing tolerances and there can be significant variation in device parameters between neighbouring qubits. These are of little consequence in classical digital logic designs because the ‘zero’ and ‘one’ logical states are usually well separated in terms of the levels used to represent them [7]. They are well-defined discrimination thresholds and they are highly robust to small fluctuations. Such classical error protection fails as the number of particles (electrons) defining a given state is reduced to the few particle level and the fragility of quantum coherence introduces new problems. Hence the Hamiltonian of each individual qubit will need to be characterized to unprecedented levels [8, 9].

Recently, attention has turned to the coupling of su-

perconducting charge qubits to microwave oscillators and resonators. This is partly motivated for the need to ‘pump’ quantum devices into excited or superposition states and partly because even pseudo-stationary control fields (static DC fields or quasi-static fields). These will have some resonant frequencies caused by the intrinsic capacitance and inductances in the connection path, this can often be approximated linear oscillators for small fluctuations and deviations. The simplest example of this is in the usual spectroscopy of the qubit where the microwave field acts as a weak probe [10], and increasing the strength of the field allows Rabi oscillations [11]. To investigate the strong-coupling limit of cavity Quantum Electrodynamics, Wallraff *et al.* constructed the analog of an optical cavity for a Cooper-Pair Box, and showed single photon dynamics [12]. This work and related theoretical analysis clearly shows the full canon of quantum optics can be translated to the superconducting arena for potential technological advantage. In addition, the ability to fabricate desired pseudo-atoms allows investigation of phenomena (particularly multi-state phenomena) that would not be convenient using conventional atoms.

We have investigated a simulated superconducting charge qubit, controlled via a classical microwave pump and a bias/control voltage. We treat the bias control as a fully quantized linear oscillator with a finite resistance (RLC oscillator) [13] which is coupled to a thermal environment [14]. The quantised oscillator is used to allow the field to represent non-adiabatic processes and entanglement between the qubit and bias field.

*Electronic address: e.j.griffith@liverpool.ac.uk

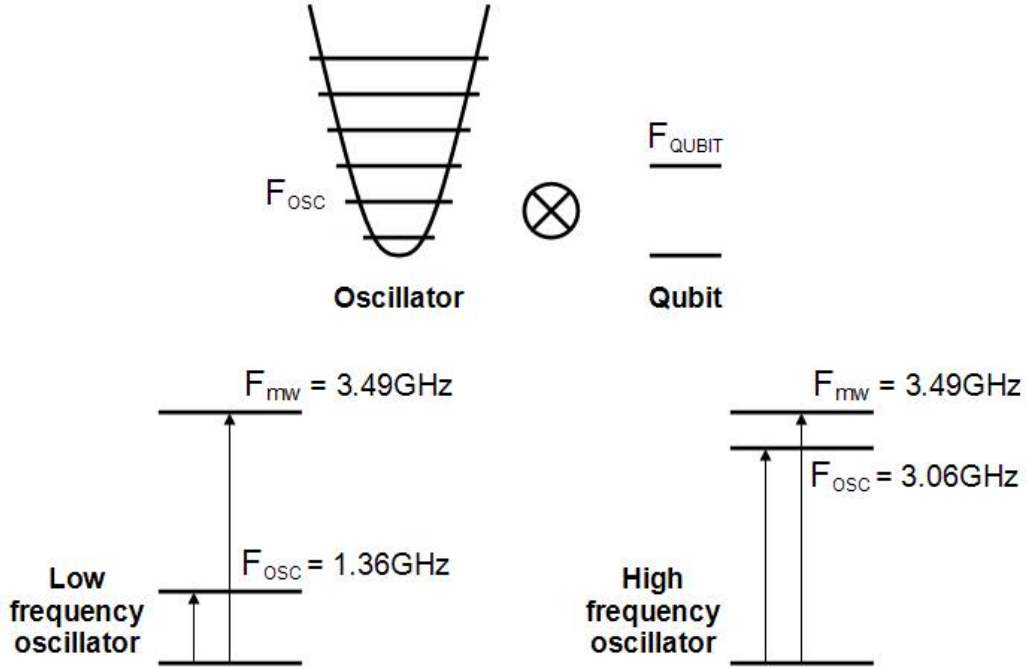


FIG. 1: The coupled qubit and oscillator system is investigated for two different qubit-oscillator detunings

System measurements can be performed on the oscillator circuit or the qubit, but measurement of the oscillator is generally preferred as it is more readily accessible via weak measurements than the fragile qubit state. One of the ways to reduce decoherence is to reduce the number degrees of freedom coupling directly to the qubit, thereby limiting the environmental noise.

In addition, the oscillator is of particular interest as its evolution is significantly affected by the qubit dynamics due to backaction caused by the two way capacitive qubit-oscillator coupling.

This paper examines the power spectral density (PSD or noise spectrum) of the oscillator and qubit as functions of the two main control parameters, microwave amplitude and bias voltage. The PSD, particularly for low sub GHz frequencies, is a readily accessible experimental measurement. By exploring non-standard parameters for the bias circuitry and microwave control, our investigations show a rich spectroscopy of dynamically controllable features. Beyond fundamental investigations, these results may be of benefit in the characterisation of qubit parameters, and the tunability of the features may allow for new control techniques for single and multiple qubit coupling [15]. These features are not restricted to superconductive devices, as semiconductor charge qubits may also exhibit similar behaviour.

We consider two situations (Fig. 1). Initially, we examine a conventional configuration in which the bias oscillator frequency is much less than both the qubit resonant frequency (Ramsey oscillations) and the microwave drive frequency. This oscillator frequency is too slow to cre-

ate excitations, so only a single set of microwave driven excitations (Rabi oscillations) are observed. The second scenario, involves using a high frequency oscillator [16] near the qubit and microwave frequencies. This smaller detuning creates a range of interesting features in the oscillator spectrum. We also observe a frequency splitting when the qubit is correctly biased in the presence of a driving signal and strong coupling. This resembles the Autler-Townes effect observed in quantum optics [17]. In this case, the oscillator frequency is sufficient to create its own excitations, which intersects and mixes with the microwave driven Rabi oscillations. This mixing allows the Rabi information to be modulated into an experimentally favourable frequency band, in addition we find that the position of this band is can be adjusted by changing the oscillator frequency.

The Autler Townes configuration is an excellent mechanism to probe the dynamics of strongly driven systems. A strongly driven transition will tend to have equal populations in each state, and hence signal to noise is compromised. In the Autler Townes configuration, the strongly driven transition is probed via a weak field on an auxiliary transition, allowing measurements of otherwise hidden dynamics to be performed. It is especially useful for probing dressed-state configurations, and has been used to monitor bichromatic [18] and polychromatically driven transitions [19, 20], V systems [21] and an all solid-state version has been proposed for charge qubit readout [22]. In our case we observe multiple side-bands corresponding to subharmonic resonances [23] and features at the multiples of the Rabi frequency [24].

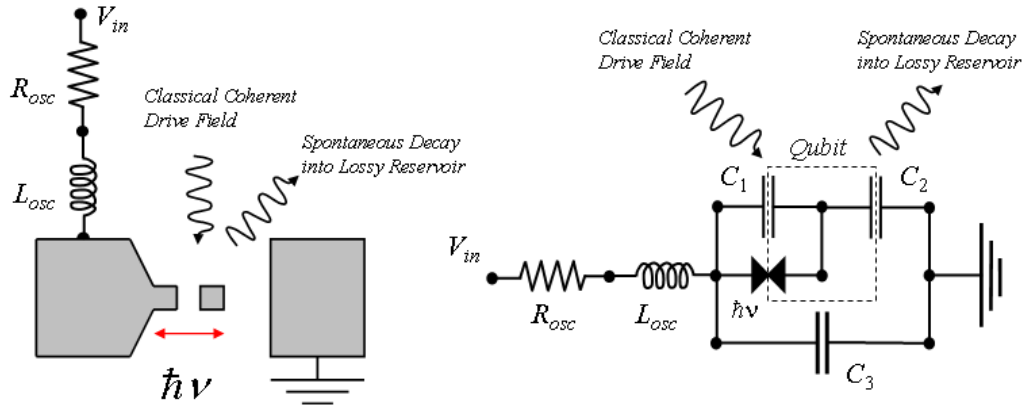


FIG. 2: Qubit geometry and equivalent electrical circuit model, showing the qubit coupled to the oscillator RLC circuit

II. SYSTEM MODEL

The system model (shown in Fig. 2) is a small superconducting island, capacitively coupled to a bulk superconductor via a Josephson junction, allowing Cooper pairs to coherently tunnel on and off the island. The Josephson junction is sufficiently weak and the total capacitance of the island sufficiently small that the energy associated with charging the island is large compared to the tunneling energy of the junction: this is normally called the Coulomb blockade regime [25]. The necessary biasing voltage is applied through the bulk superconductor, across the Josephson junction. In addition, the qubit is also coupled capacitively to a grounding electrode, defining a reference point for the junction biasing voltage.

The bias circuit has natural intrinsic dynamics with

a characteristic frequency response, we approximate this by a resonant RLC oscillator in series with the island, which takes into account the intrinsic inductance and capacitance present in the bias circuit, as well as a parasitic capacitance across the bias electrodes. This oscillator is modelled quantum mechanically as a standard N -state Simple Harmonic Oscillator (SHO) allowing non-adiabatic processes and not limiting the analysis to low frequency fields [26, 27, 28, 29]. The bias oscillator is also connected to an external amplifier through which the oscillator voltage can be measured. The qubit charge state can be inferred from its reactive backreaction on the oscillator charge, and thereby its voltage.

The presence of fluctuations in the oscillator will have an effect on the qubit, as an additional source of environmental decoherence, but this can be minimised by maintaining a suitably low temperature (10mK).

The Hamiltonian for this coupled system is:

$$H = \frac{q^2}{2C_q} + \kappa \frac{qQ}{C_q} + \frac{Q^2}{2C_Q} + V_{in}Q + \frac{\Phi^2}{2L_{osc}} - \hbar\nu \sin\left(2\pi \frac{\theta}{\Phi_0}\right) \quad (1)$$

with capacitances and coupling parameter κ given by:

$$C_q = \frac{C_1C_2 + C_2C_3 + C_3C_1}{C_2 + C_3} \quad (2a)$$

$$C_{qQ} = \frac{C_1C_2 + C_2C_3 + C_3C_1}{2C_2} \quad (2b)$$

$$C_Q = \frac{C_1C_2 + C_2C_3 + C_3C_1}{C_1 + C_2} \quad (2c)$$

$$\kappa = \frac{C_q}{2C_{qQ}} \quad (2d)$$

TABLE I: Table of typical component values

	Description	Typ.
$\nu/2\pi$	Josephson energy	1.94GHz
C_1	Josephson junction capacitance	500aF
C_2	Qubit-Grounded Bulk capacitance	500aF
C_3	Parasitic capacitance formed between the bulk electrodes	500fF
L_{osc}	Biassing circuit inductance	27.4nH
R_{osc}	Biassing circuit resistance	1.17Ω

The qubit geometry is transformed to a classical electrical circuit model (Fig. 2). The circuit includes the intrinsic qubit capacitances C_1 and C_2 , (the Josephson junction capacitance and a grounded bulk connection capacitance). In addition, a large parasitic capacitance C_3 is formed between the bulk superconductor electrodes and is connected to the inductive and resistive elements of the biasing circuit.

The Hamiltonian is derived from consideration of circuit voltage and current laws [30], with the Josephson junction current given by the well known phase-current relation (Eq. 3) where θ is the superconducting phase difference between the adjoining segments.

$$I_J = I_C \sin\left(2\pi\frac{\theta}{\Phi_0}\right) \quad (3)$$

The resulting Hamiltonian (Eq. 1) is rewritten to separate the qubit (\hat{q}) and oscillator (\hat{Q}) degrees of freedom, and a coupling constant κ is introduced. The κ term (Eq. 4) is typically very much less than one, and in the limit $\kappa \rightarrow 0$ the cross-coupling qQ term is zero and the systems evolve independently.

$$\kappa^2 \frac{C_Q}{C_q} \ll 1 \quad (4)$$

In addition, it should be noted that the capacitances C_1, C_2, C_3 have been redefined as effective qubit and bias oscillator capacitances, C_q, C_{qQ}, C_Q , (Eq. 2). The term $V_{in}Q$ is the contribution of the bias/control voltage and the inductive term arises from the magnetic flux associated with the oscillator geometry.

Starting from equation 1 it is possible to group the Hamiltonian terms into three parts: the oscillator and qubit Hamiltonians together with a coupling term (Eq. 5).

$$H = H_{osc} \otimes I_{qubit} + I_{osc} \otimes H_{qubit} + H_{coupling} \quad (5)$$

Each part is then quantised to a matrix representation. The combined quantised system Hamiltonian is presented here (Eqs. 7, 9, 12). Where $\delta_{m_\alpha, n_\alpha}$ represents a non-zero element in a $2N \times 2N$ matrix, where suffixes $\alpha = 1$ and $\alpha = 2$ denote the oscillator and qubit basis respectively.

1. Oscillator Hamiltonian, H_{osc}

The oscillator is quantised as a simple harmonic oscillator (Eq. 6), with energy ω . In the electrical circuit model, the charge \hat{Q} and flux $\hat{\Phi}$ form the conjugate variables, analogous to momentum (\hat{p}) and position (\hat{x}), (Eq. 6a). We also assume if the qubit is maintained at a suitably low temperature (10mK) the contributions of the higher energy levels ($m_1, n_1 \gg N$) are insignificant, hence we constrain the system to the lowest N oscillator states

for computational efficiency.

$$H_{osc} = \frac{\hat{\Phi}^2}{2L_{osc}} + \frac{\hat{Q}^2}{2C_Q} \equiv \frac{1}{2}k\hat{x}^2 + \frac{\hat{p}^2}{2m} \quad (6a)$$

$$E_n = \hbar\omega \left(n + \frac{1}{2}\right), \quad \omega = \sqrt{\frac{1}{LC}} \quad (6b)$$

$$H_{osc} = \hbar\omega \left(n_1 + \frac{1}{2}\right) \delta_{m_1, n_1} \delta_{m_2, n_2} \quad (7)$$

Where, in this paper, $\omega/2\pi$ is 1.36GHz for the low frequency oscillator with 3.06GHz being the high oscillator frequency.

2. Qubit Hamiltonian, H_{qubit}

The qubit basis is defined as the presence or absence of a single Cooper pair on the island, $0e$ and $2e$. Although there may be higher states present, we assume the probability of a third state is negligible.

$$H_{qubit} = \frac{\hat{q}^2}{2C_q} - \hbar\nu \cos\left(2\pi\frac{\hat{\theta}}{\Phi_0}\right) \quad (8a)$$

$$H_{qubit} = \frac{2e^2}{C_q} |1\rangle\langle 1| - \frac{\hbar\nu}{2} (|0\rangle\langle 1| + |1\rangle\langle 0|) \quad (8b)$$

$$H_{qubit} = \delta_{m_1, n_1} \left(\frac{2e^2}{C_q} \delta_{m_2, 1} \delta_{n_2, 1} - \frac{\hbar\nu}{2} (\delta_{m_2, 1} \delta_{n_2, 0} + \delta_{m_2, 0} \delta_{n_2, 1}) \right) \quad (9)$$

The biasing field $V_{in}Q$ together with the microwave field is applied as an effective qubit charge q_{ext} , which modifies the qubit basis \hat{q} .

$$q_{ext}(t) = Q_{bias} + A_{mw} \sin(\omega_{mw}t) \quad (10a)$$

$$\hat{q}(t) = q_{ext} |0\rangle\langle 0| + (q_{ext} + 2e) |1\rangle\langle 1| \quad (10b)$$

3. Coupling term, $H_{coupling}$

The qubit-oscillator coupling term is the product of the qubit and oscillator charge operators. To quantise this we express the oscillator charge \hat{Q} in terms of raising and lowering operators [13]. The terms $\sqrt{n_1}$ and $\sqrt{n_1 + 1}$ are normalisations for the changes in oscillator state.

$$H_{coupling} = \kappa \frac{\hat{q}\hat{Q}}{C_q} \quad (11a)$$

$$\hat{Q} = -i\sqrt{\frac{\hbar m\omega}{2}} (a - a^\dagger) \quad (11b)$$

$$H_{coupling} = -i \frac{\kappa e}{C_q} \sqrt{2\hbar m\omega} \delta_{m_2, 1} \delta_{n_2, 1} \times (\sqrt{n_1} \delta_{m_1, n_1} - \sqrt{n_1 + 1} \delta_{m_1, n_1 + 1}) \quad (12)$$

III. UNRAVELLINGS AND WEAK MEASUREMENTS

The evolution of the quantum system (qubit and oscillator) in the presence of environmental fluctuations is described by the usual master equation.

$$\frac{d\rho}{dt} = -i[H, \rho] + \sum_m \left(L_m \rho L_m^\dagger - \frac{1}{2} L_m^\dagger L_m \rho - \frac{1}{2} \rho L_m^\dagger L_m \right) \quad (13)$$

where $\rho = |\psi\rangle\langle\psi|$ is the density operator for the combined system.

Unravelling the master equation allows us to represent only the stochastic effects within the qubit and oscillator as a whole. In this section we describe two unravellings which correspond to spontaneous emissions and the thermal diffusion mechanism of the oscillator. This environment also includes the effects of an external measuring system on the oscillator as this will add to the decoherence. We have chosen a quantum state diffusion (QSD) unravelling to model oscillator dissipation, although equally valid is the quantum jump (QJ) unravelling representing a different measurement process on the environment, indeed both unravellings should agree on average [31].

A. Oscillator quantum state diffusion

Quantum state diffusion is applied to simulate the effects of a finite temperature environment, and dissipation [14]. The diffusion model consists of random thermal and quantum fluctuations combined with a progressive drift of the quantum state. The system stochastic evolution is now governed by equation 14.

$$\begin{aligned} |d\psi\rangle &= -\frac{i}{\hbar} H |\psi\rangle dt \\ &+ \sum_m \left(\langle L_m^\dagger \rangle_\psi L_m - \frac{1}{2} L_m^\dagger L_m - \frac{1}{2} \langle L_m^\dagger \rangle_\psi \langle L_m \rangle_\psi \right) |\psi\rangle dt \\ &+ \sum_m (L_m - \langle L_m \rangle) |\psi\rangle d\xi_m \end{aligned} \quad (14)$$

where $d\xi_m$ are independent complex differential random variables (Weiner increments), which satisfy:

$$E(d\xi_m) = 0 \quad (15a)$$

$$E(d\xi_n d\xi_m) = 0 \quad (15b)$$

$$E(d\xi_n^* d\xi_m) = \delta_{nm} dt \quad (15c)$$

For the arbitrary index $m = 1, 2$ we define two environment operators $L_m = L_1, L_2$, [14].

$$L_1 = \sqrt{(\bar{n} + 1) \frac{\omega}{Q_D}} a \quad (16a)$$

$$L_2 = \sqrt{\bar{n} \frac{\omega}{Q_D}} a^\dagger \quad (16b)$$

$$\bar{n} = \frac{1}{\exp(\frac{\hbar\omega}{kT}) - 1} \quad (16c)$$

where Q_D is the quality factor of the oscillator and is proportional to the dissipative elements, \bar{n} is the average oscillator occupancy and ω is the angular frequency of the oscillator. The oscillator occupancy is dependent on the thermal temperature of the environment which is assumed constant at $T=10\text{mK}$.

B. Qubit quantum jumps

To model the spontaneous photon emissions from the qubit as it undergoes a modified Schrödinger evolution we adapt a quantum jump trajectory unravelling found in quantum optics [32]. We allow the qubit to emit a photon into a dissipative reservoir (experimental cavity), in which it is immediately absorbed (measured). If we apply continuous quantum measurements to the qubit we require two measurement operators (Eq. 17), the subscript indicates the emission and absorption of a photon (i.e. a jump has occurred).

$$\Omega_0(dt) = 1 - \frac{i}{\hbar} H dt - \frac{\gamma}{2} \sigma^\dagger \sigma dt \quad (17a)$$

$$\Omega_1(dt) = \sqrt{\gamma dt} \sigma \quad (17b)$$

where $\sigma = |0\rangle\langle 1|$, while γ sets the jump rate so that $\gamma \langle \sigma^\dagger \sigma \rangle$ is the actual photon emission rate, ($\gamma = 0.05 f_{osc}$ which implies 0.05 jumps per bias oscillator period). Equation 17a represents the continuous evolution of the qubit state over the interval dt , whereas equation 17b describes the collapse of the state when a quantum jump has occurred.

Over each simulation interval, dt , the state is updated via one of two equations (Eq. 18) dependent on the result of an instantaneous weak measurement, in normal evolution equation 18a is used, however if a jump occurs a '1' will be measured (photon emitted) and equation 18b should then be used and the state renormalised.

$$|\psi_0(t+dt)\rangle = \Omega_0(dt) |\psi(t)\rangle \quad (18a)$$

$$|\psi_1(t+dt)\rangle = \Omega_1(dt) |\psi(t)\rangle \quad (18b)$$

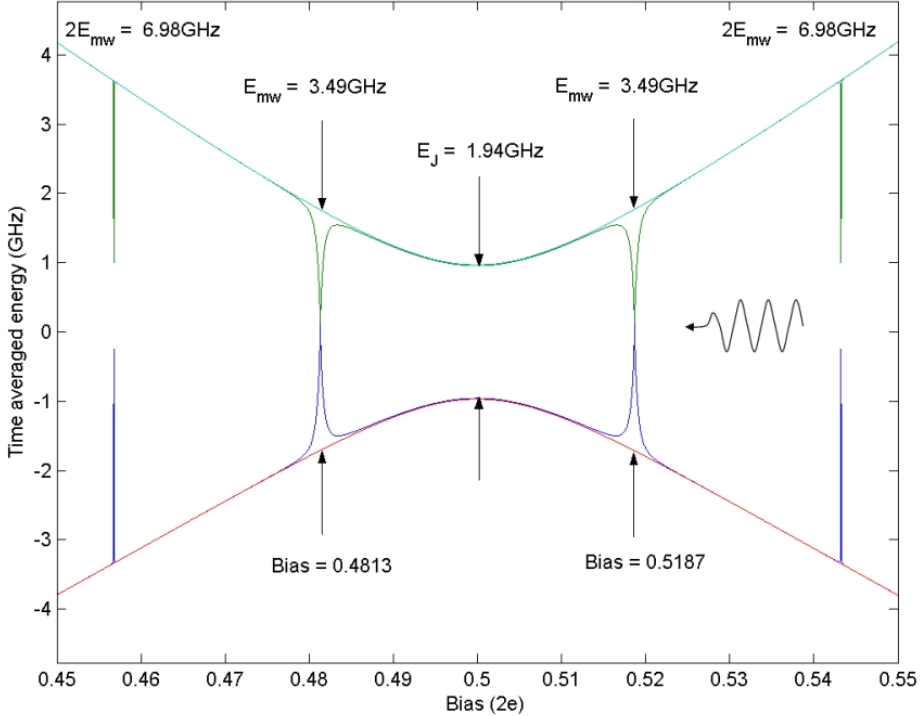


FIG. 3: Time averaged Floquet qubit energy levels, with one and two photon microwave transitions (3.49GHz and 6.98GHz)

IV. ENERGY LEVEL STRUCTURE

It is useful to be able to quantify several important qubit parameters, as the qubit behaviour is particularly sensitive to parameter variation. These arise from the manufacturing techniques used, which have often been driven by industrial goals of delivering cheap yet inaccurate components. It is important to understand that small variations in the capacitive coupling can have a significant effect on the system behaviour. These errors could occur through a variety of real situations. For example, overlaps between layers in the epitaxially grown structure, intrinsic parasitic capacitances such as fringe effects, or defects in the Josephson junctions [33]. Unfortunately whilst these variations can be kept to a minimum by improved design and lithography, we cannot expect perfect structures, and once integrated and fabricated we cannot measure every capacitance directly. Instead, we are likely to require methods to remotely characterise the qubit in circuit.

The qubit behaviour is partially characterised by the energy level diagram (Fig. 3) [34, 35], which also shows the time averaged (Floquet) energy levels for the microwave driven qubit [36]. The Floquet energies are a useful illustration of where transitions can occur for a particular microwave drive frequency. However, this is

not necessarily known and cannot be assumed to be identical for all qubits.

Indeed, techniques have been proposed to deduce the energy level structure from measurements of peak noise power in the biasing circuit, caused when the qubit is correctly biased with the injected microwave field [26, 27, 28]. The system described in this paper is driven with a 3.49GHz microwave, which gives rise to a transition between the energy levels, the width of which becomes wider as the microwave amplitude (A_{mw}) is increased. The single photon (3.49GHz) transition occurs symmetrically near two bias points (0.4812 and 0.5187). We have chosen to operate about the upper bias point (0.5187), although identical features would be present near the lower point. Two photon transitions occur at 6.96GHz, although the bias required to utilise these transitions are far above our parameter range, so their effects will be ignored.

The graph also clearly shows the expected avoided crossing caused by the Josephson junction, with an energy separation, E_J (1.94GHz), transitions cannot occur for microwaves driving below this frequency. This is important, as only the 3.06GHz high frequency biasing oscillator should be sufficient to create the excitations that interfere with the microwave and cause the many strong and interesting features, unlike the 1.36GHz low frequency oscillator circuit.

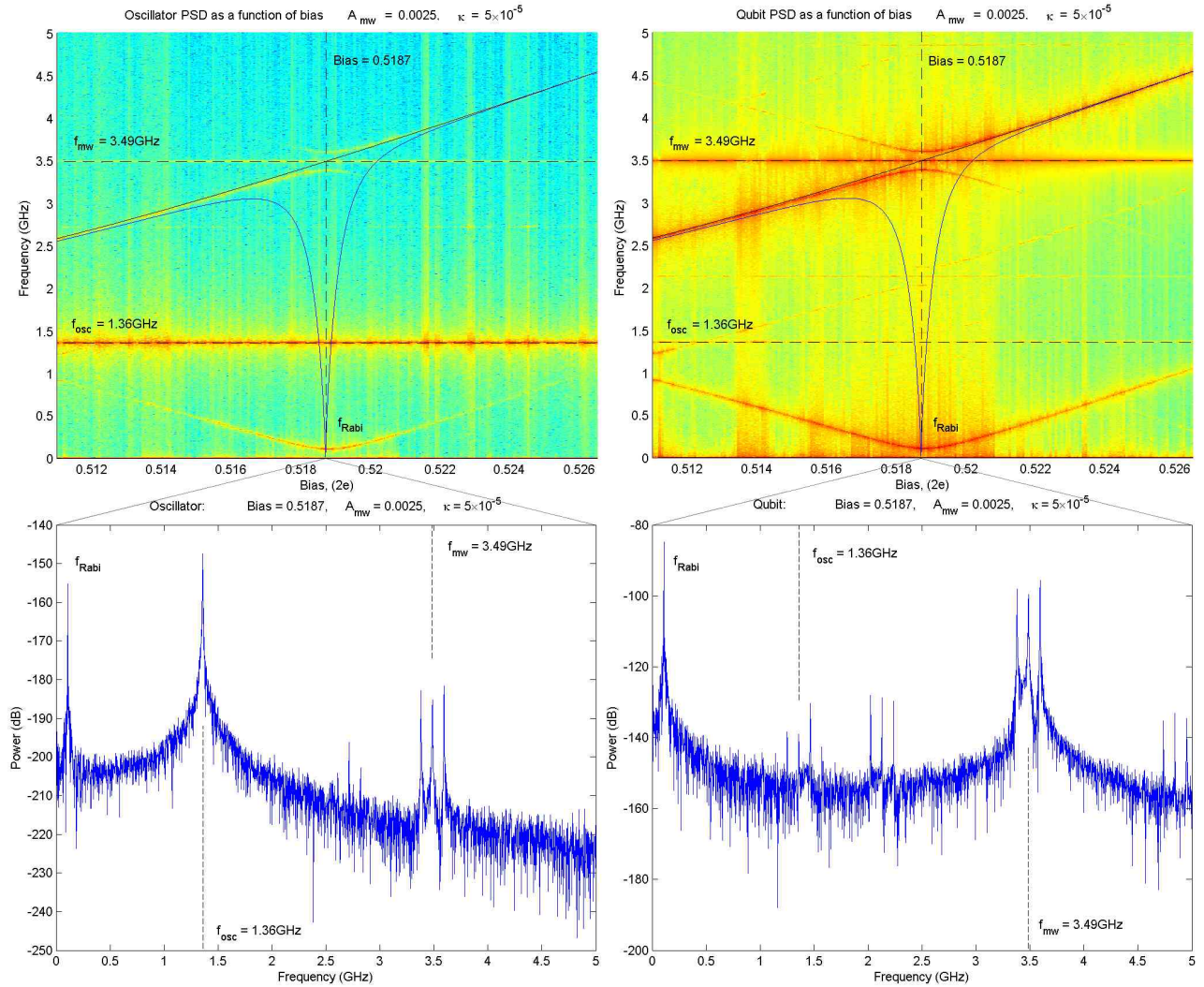


FIG. 4: Oscillator and Qubit power spectra slices for Bias = 0.5187, using low frequency oscillator circuit $f_{osc} = 1.36\text{GHz}$

V. FREQUENCY SPECTRA

In this section we consider the frequency spectrum of the system, or the power spectral density (PSD) which is an experimentally measurable quantity. The power spectral density reveals the strength of the frequencies present in a time varying signal. In this case the signals are voltages, which are calculated from the expectation values of qubit and oscillator charge. The expectation values are obtained using the reduced density operator for the qubit and oscillator basis, applying the relevant charge operator and then tracing the result $\langle q \rangle = Tr \{ \hat{q} \rho \}$.

In the example figure (Fig. 4), the control bias is varied from left to right for a low frequency oscillator circuit (1.36GHz). For each bias point the simulation is reinitialised, the stochastic time evolution of the oscillator and qubit are extracted to obtain the power spectrum for each component, with a frequency resolution of 4.01MHz. The power spectra for each time series are collated as

an image such that the power axis is now represented as a colour, and the individual power spectra are vertical ‘slices’ through the image. The dominant frequency peaks become line traces, therefore illustrating the various avoided crossings, mergeings and intersections. The example figure shows the PSD ‘slice’ at Bias = 0.5187, the broadband noise is readily apparent and is due to the discontinuous quantum jumps in the qubit. The bias oscillator peak (1.36GHz) is most prominent in the oscillator PSD, as would be expected, but it is also present in the qubit PSD. It should also be noted that most features are present in both the qubit and oscillator. Interestingly, the qubit PSD is significantly stronger than the oscillator PSD, however the larger voltage is generated by the smaller charge due to the extremely small island capacitance.

In addition, the energy level separation (Fig. 3) has been overlaid as a solid curved line to illustrate the effect of the microwave drive.

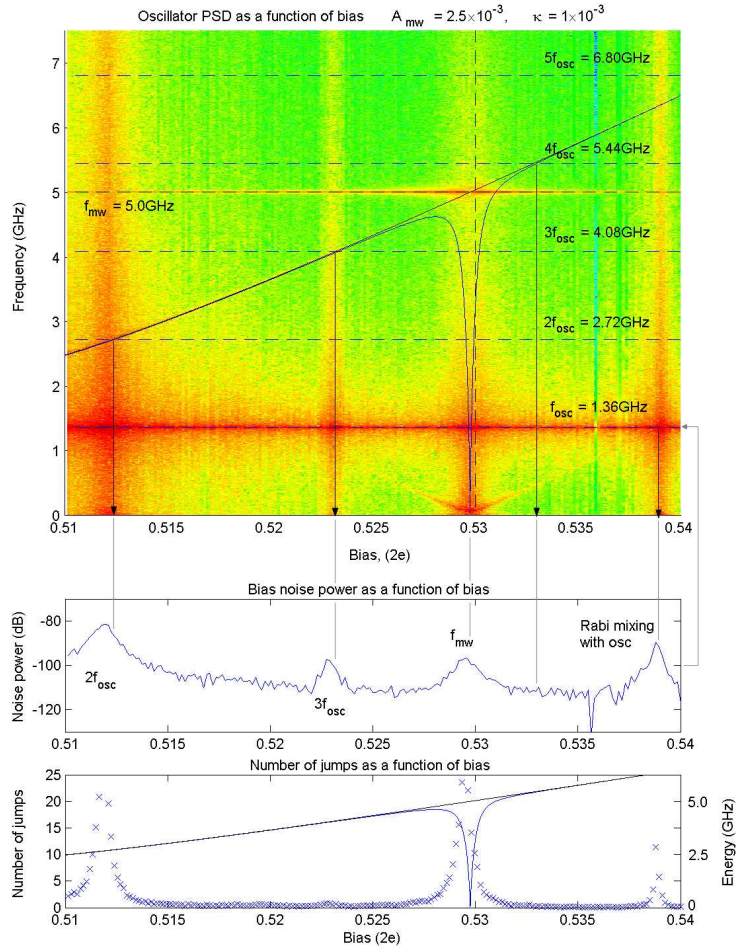


FIG. 5: Run averaged oscillator power spectra for $f_{mw} = 5\text{GHz}$, showing bias noise power at $f_{osc} = 1.36\text{GHz}$

In a previous paper [26], a method was proposed by which the energy level structure of a charge qubit can be obtained from measurements of the peak noise in the bias/control oscillator. This was based on a technique originally proposed for superconducting flux qubits [26] but there are many similarities between the two technologies. The oscillator noise peak is the result of broadband noise caused by quantum jumps in the qubit being coupled back to the oscillator circuit. This increase in the jump rate becomes a maximum when the Rabi oscillations are at peak amplitude, this should only occur when the qubit is correctly biased and the microwave drive is driving at the transition frequency. Therefore by monitoring this peak as a function of bias, we can associate a bias position with a microwave frequency equal to that of the energy gap, hence constructing the energy diagram (Fig. 3). The extra peaks are due to oscillator harmonics driving the qubit, however the far right peak is due to resonance between the Rabi oscillations and the bias oscillator.

The previous work assumed a classical oscillator model, we show in this paper that it also holds true for a quan-

tised oscillator circuit. Although the effect is weaker, it should still be detectable as the peak is +10dB to +15dB above the background noise (Fig. 5).

The next two sections illustrate how the two control fields affect the features, by first using the above mentioned method for determining the energy level structure, it may be possible to determine the *true* bias and microwave fields applied to the qubit:

- Section A investigates the effect of *sweeping the bias field* about the energy level transition, for a constant microwave frequency of 3.49GHz.
- Section B investigates the effect of *sweeping the microwave frequency*, at a constant bias of 0.5187.

In both sections, the example figures provided use the high frequency (3.06GHz) bias oscillator. This higher frequency bias field requires a quantum oscillator model because the classical model is insufficient [29]. To illustrate the additional effects created when two frequencies are driving in close proximity, it is necessary to compare the following plots with figure 4. In addition the coupling, κ is kept constant at 5×10^{-5} .

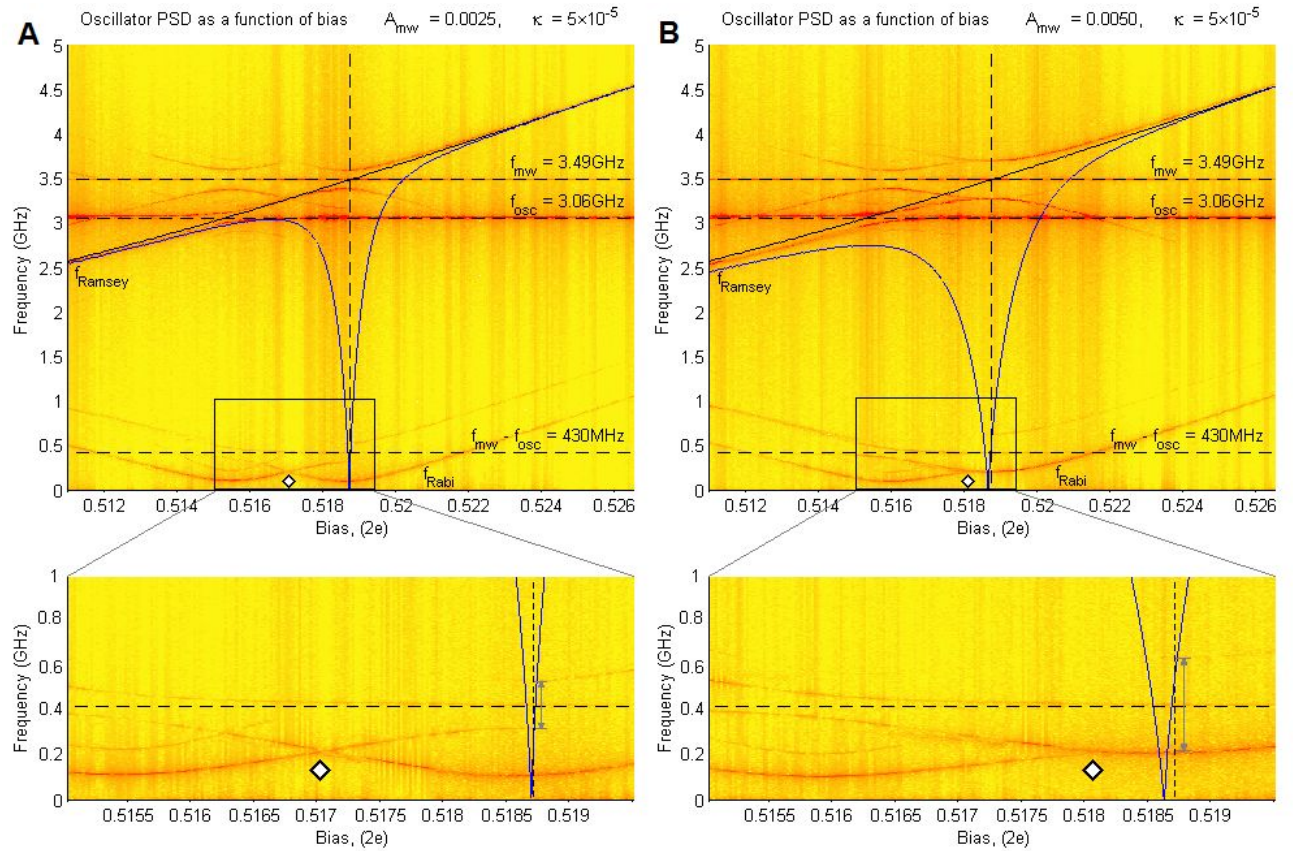


FIG. 6: Oscillator PSD as a function of bias, for microwave amplitudes $A_{mw} = 0.0025$ (A) and $A_{mw} = 0.0050$ (B)

A. Bias field sweep

Figure 6 shows plots of the PSD for two different microwave amplitudes $A_{mw} = 0.0025$ (A) and $A_{mw} = 0.0050$ (B) driving at 3.49GHz with a high frequency bias oscillator of 3.06GHz.

Although not shown, when the microwave field is removed there are still some effects due to the 3.06GHz high frequency oscillator causing excitations and a splitting in the qubit. This is possible as the oscillator exceeds the Josephson junction frequency (1.94GHz) and so drives the qubit as per an injected microwave field. Alternatively, if a low frequency oscillator (1.36GHz) is used, there are no excitations and the Ramsey oscillations remain undisturbed, unless the qubit is biased on a harmonic of the oscillator, which would therefore exceed the Josephson frequency and start driving the qubit.

When the microwave is applied we notice interesting effects, arising from the additional interference of the ‘side bands’ created by the 3.06GHz oscillator drive signal, which is now in close proximity to the 3.49GHz microwave field. This relatively small detuning causes a multitude of splittings, similar to that of the Autler-Townes effect [18]. However, this is a benefit as it creates many more features in the frequency spectrum, which in

turn increases the information that can be gained.

The mixing of the Rabi oscillations with the microwave field causes ‘side bands’ surrounding the drive signal. It is important to note that the high frequency behaviour surrounding the drive signals is replicated at $f_{mw} - f_{osc} = 430\text{MHz}$, and this area of interest has been enlarged, indeed, this should be an easily accessible frequency range. This frequency regime can be adjusted on to an experimental bandwidth by changing the oscillator frequency, and hence the aforementioned separation, $f_{mw} - f_{osc}$.

In addition, within the PSD there exists a point of interest (\diamond) where the microwave and oscillator excitations intersect. As the hyperbolic shape of the oscillator excitations remains quite constant for low amplitude microwaves, the intersection point will mainly be governed by the amplitude and frequency of the microwave. It can be seen in plot A, when the microwave is driving at equal intensity to the oscillator ($A_{mw} = 0.0025$), the intersection occurs halfway between the two signals. Hence it may be possible to characterise the oscillator in terms of microwave properties, and furthermore estimate the effects or significance of the oscillator energy transition. Indeed, for high microwave amplitudes ($A_{mw} > 0.0050$), the microwave transition width eventually increases to enclose the oscillator transition, then the features merge.

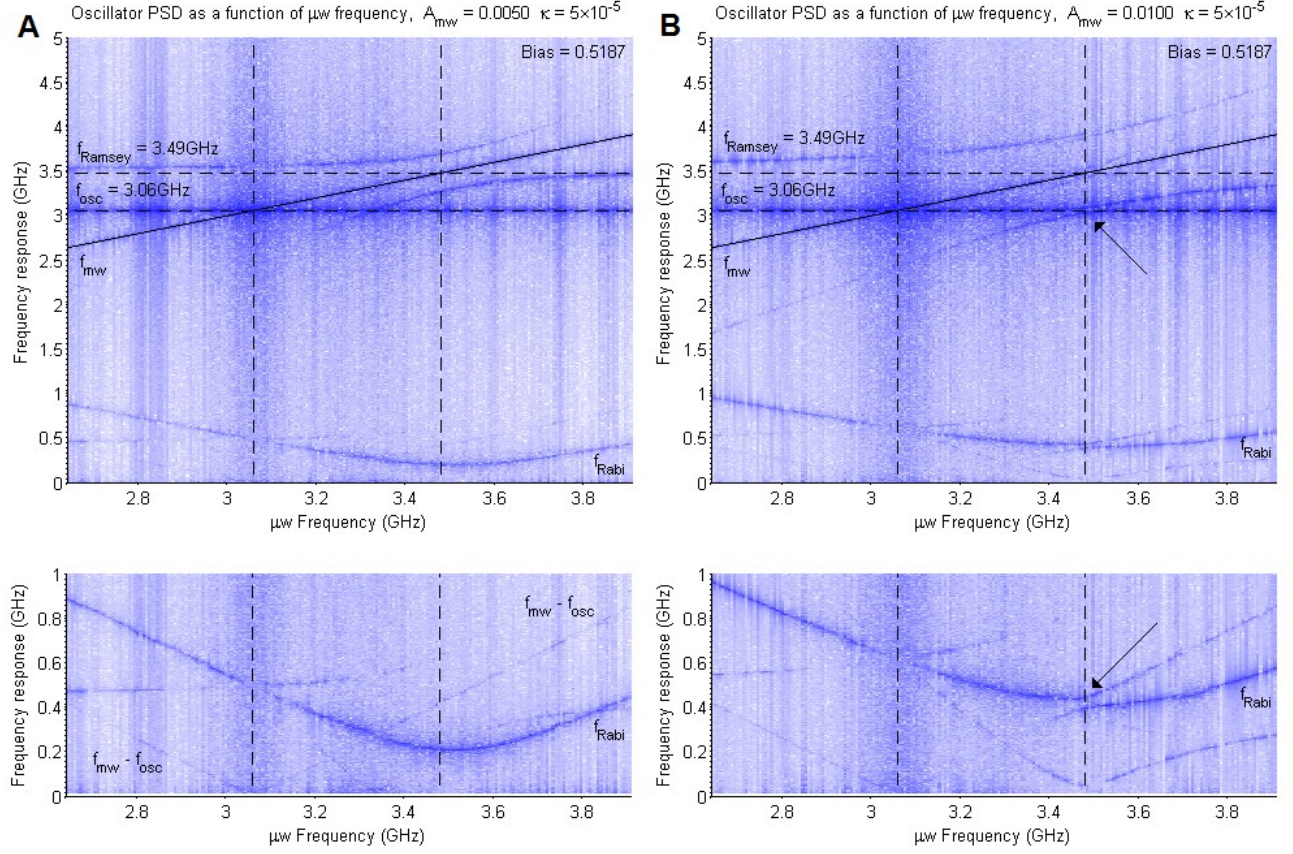


FIG. 7: Oscillator PSD as a function of f_{mw} , for microwave amplitudes $A_{mw} = 0.0050$ (A) and $A_{mw} = 0.0100$ (B)

B. Microwave frequency sweep

Figure 7 is presented as the two dimensional plots described previously. However there are now two frequency axes: the horizontal axis represents the frequency of the applied microwave drive field, and the vertical axis is the frequency response. It should be remembered that the microwave frequency axis is focused on the transition frequencies and *the diagonally increasing line is now the microwave frequency*, not the Ramsey oscillations.

The most interesting features in question are secondary splittings, which occur only when the lower Rabi side-band passes through the oscillator peak, splitting it. The oscillator frequency split is somewhat obscured by the large oscillator peak, however the low frequency splitting centred on $f_{mw} - f_{osc} = 430\text{MHz}$ is clearly visible in the magnified section, as indicated by the arrows.

We find by changing the microwave amplitude and hence the Rabi side-band separation, the particular combination required to cause maximum splitting only occurs for the Rabi oscillations with maximum amplitude, which is set by the bias field. Hence the microwave amplitude and a feature in frequency space can be related. The lines (traces) created by these splitting effects can be observed at a given applied microwave frequency, the

traces expand and contract dependant on the proximity of the splitting. Therefore by tracking the expansion of these traces it may be possible to tune the microwave amplitude until the Rabi frequency is required.

This could be applied to calibrate the microwave waveguide, in which one could determine the effective microwave applied to the qubit in terms of the microwave amplitude applied at the external end of the waveguide. This is important as the characteristics of the waveguide, such as impedance, are frequency dependant. If the separation of the two known frequencies is fixed, (the oscillator and the microwave), we know by maximising the secondary splitting using the microwave amplitude that the Rabi side-band must now be equal to the well defined oscillator-microwave frequency separation, and therefore the external microwave amplitude that caused it. In addition, the maximum splitting solution should indicate a correctly biased system.

If the oscillator were of a much lower frequency (1.36GHz) then only the Rabi oscillations and Rabi side-bands would appear (Fig. 4), and none of these additional interactions would exist. The extra features caused by this small detuning is an important point to reinforce as it links the microwave, oscillator, Rabi oscillations and bias field together.

VI. CONCLUSION

In this paper we have presented features that exist within the power spectra of a charge qubit. The qubit is coupled via a single Josephson junction to a (fully quantised) oscillator circuit, which provides a bias voltage and a means of measurement. A quantum trajectory approach has been used, with the quantum state diffusion unravelling of the master equation simulating a dissipative oscillator, and a quantum jumps unravelling simulates spontaneous emissions from the qubit to a lossy reservoir.

We have confirmed that previous work involving a classical bias oscillator still holds for a quantised model, although the response is weaker than expected, it is still significant and should be detectable in experimental systems. This technique is intended to allow the energy level separation of a charge qubit to be measured in-situ and with the minimum of measuring circuitry. We also report additional features that are created in the power spectrum of the qubit (and the coupled oscillator) when the oscillator resonant frequency and microwave frequency are similar (3.06GHz and 3.49GHz respectively). These features are predominantly discontinuous frequency splittings akin to the Autler-Townes effect in quantum optics, and the intersections of frequency peaks as functions of the control fields. These effects are also present at low

(sub GHz) frequencies which are expected to be more easily accessible by experiment than the original 2 to 4 GHz frequency range. This frequency range can be moved into an experimental bandwidth by adjusting the oscillator frequency.

The close proximity of a second drive field (the oscillator), to the microwave drive adds information to the noise spectra and allows access to other features, by searching for frequency separations and discontinuities we can identify bias settings and new amplitudes from artefacts in the frequency domain.

Acknowledgements

The authors would like to thank Drs. P. J. Meeson, M. J. Everitt and J. H. Cole for helpful comments and suggestions.

E. J. Griffith is supported by a Department of Electrical Engineering and University of Liverpool scholarship. A. D. Greentree is supported by the Australian Research Council, the Australian government and by the US National Security Agency (NSA), Advanced Research and Development Activity (ARDA) and the Army Research Office (ARO) under contract number W911NF-04-1-0290.

[1] Y. Nakamura, Y. A. Pashkin, and J. S. Tsai, *Nature*. **398**, 786 (1999).

[2] E. Paladino, F. Taddei, G. Giaquinta, and G. Falci, *Physica E* **18**, 39 (2003).

[3] O. Astafiev, Y. A. Pashkin, T. Yamamoto, Y. Nakamura, and J. S. Tsai, *Phys. Rev. B* **69**, 180507 (2004).

[4] Y. A. Pashkin, T. Yamamoto, O. Astafiev, Y. Nakamura, D. V. Averin, and J. S. Tsai, *Nature*. **421**, 823 (2003).

[5] B. E. Kane, *Nature*. **393**, 113 (1998).

[6] J. Q. You, J. S. Tsai, and F. Nori, *Phys. Rev. Lett.* **89**, 197902 (2002).

[7] J. R. Gibson, *Electronic logic circuits* (Arnold, 1992), 3rd ed.

[8] S. G. Schirmer, A. Kolli, and D. K. L. Oi, *Phys. Rev. A* **69**, 050306(R) (2004).

[9] J. H. Cole, S. G. Schirmer, A. D. Greentree, C. J. Wellard, D. K. L. Oi, and L. C. L. Hollenberg, *Phys. Rev. A* **71**, 062312 (2005).

[10] Y. Nakamura, C. D. Chen, and J. S. Tsai, *Phys. Rev. Lett.* **79**, 2328 (1997).

[11] Y. Nakamura, C. D. Chen, and J. S. Tsai, *Phys. Rev. Lett.* **87**, 246601 (2001).

[12] A. Wallraff, D. I. Schuster, A. Blais, L. Frunzio, R.-S. Huang, J. Majer, S. Kumar, S. M. Girvin, and R. J. Schoelkopf, *Nature*. **431**, 162 (2004).

[13] D. K. Ferry, *Quantum Mechanics: An Introduction for Device Physicists and Electrical Engineers* (Institute of Physics Publishing, 2000), 2nd ed.

[14] T. P. Spiller, B. M. Garraway, and I. C. Percival, *Phys. Lett. A* **179**, 63 (1993).

[15] J. F. Ralph, E. J. Griffith, T. D. Clark, and M. J. Everitt, *Phys. Rev. B* **70**, 214521 (2004).

[16] E. K. Irish, J. Gea-Banacloche, I. Martin, and K. C. Schwab, *ArXiv Condensed Matter e-prints* (2004), arXiv:cond-mat/0412392.

[17] S. H. Autler and C. H. Townes, *Phys. Rev.* **100**, 703 (1955).

[18] A. D. Greentree, C. Wei, S. A. Holmstrom, J. P. D. Martin, N. B. Manson, K. R. Catchpole, and C. Savage, *J. Opt. B: Quantum Semiclass. Opt.* **1**, 240 (1999).

[19] A. D. Greentree, C. Wei, and N. B. Manson, *Phys. Rev. A* **59**, 4083 (1999).

[20] S. Papademetriou, M. F. V. Leeuwen, and J. C. R. Stroud, *Phys. Rev. A* **53**, 997 (1996).

[21] S. R. de Echaniz, A. D. Greentree, A. V. Durrant, D. M. Segal, J. P. Marangos, and J. A. Vaccaro, *Phys. Rev. A* **64**, 013812 (2001).

[22] A. D. Greentree, A. R. Hamilton, and F. Green, *Phys. Rev. B* **70**, 041305(R) (2004).

[23] G. Agarwal and N. Nayak, *Phys. Rev. A* **33**, 391 (1986).

[24] A. S. M. Windsor, C. Wei, S. A. Holmstrom, J. P. D. Martin, and N. B. Manson, *Phys. Rev. Lett.* **80**, 3045 (1998).

[25] I. L. Aleiner, P. W. Brouwer, and L. I. Glazman, *Phys. Rep.* **358**, 309 (2002).

[26] J.F.Ralph, T.D.Clark, M.J.Everitt, H.Prance, P.Stiffell, and R.J.Prance, *Phys. Lett. A* **317**, 199 (2003).

[27] E.J.Griffith, J.F.Ralph, and T.D.Clark, *Proc. AIP* **723**, 401 (2004).

[28] J.F.Ralph, E.J.Griffith, T.D.Clark, M.J.Everitt, and

P.Stiffell, Proc. SPIE Vol. **5436**, 242 (2004).

[29] T. P. Spiller, T. D. Clark, R. J. Prance, and H. Prance), Phys. Lett. A **170**, 273 (1992).

[30] G. Burkard, Phys. Rev. B **71**, 144511 (2005).

[31] T. A. Brun, N. Gisin, P. F. O'Mahony, and M. Rigo, Phys. Lett. A **229**, 267 (1997).

[32] H. Wiseman and G. Toombes, Phys. Rev. A **60**, 2474 (1999).

[33] H. G. Kerkhoff and A. A. Joseph, Proc. IEEE (DELTA 2004) pp. 9–14 (2004).

[34] J. R. Friedman, V. Patel, W. Chen, S. K. Tolpygo, and J. E. Lukens, Nature. **406**, 43 (2000).

[35] M. O. Scully and M. S. Zubairy, *Quantum Optics* (Cambridge University Press, 1997).

[36] T. D. Clark, J. Diggins, J. F. Ralph, M. Everitt, R. J. Prance, H. Prance, R. Whiteman, A. Widom, and Y. N. Srivastava, Ann. Phys. **268**, 1 (1998).